Synthetic 3D inversion of tidally induced magnetic field

Libor Šachl, Jakub Velímský

6.1. 2021

Current section

1 Introduction

2 Forward and inverse modelling

3 Numerical setup

4 Results

Wind and buoyancy driven ocean circulation

- driven by wind stresses and pressure gradients
- surface and deep (= meridional overturning = thermohaline) circulation
- average horizontal velocities 0.01 - 0.1 m/s

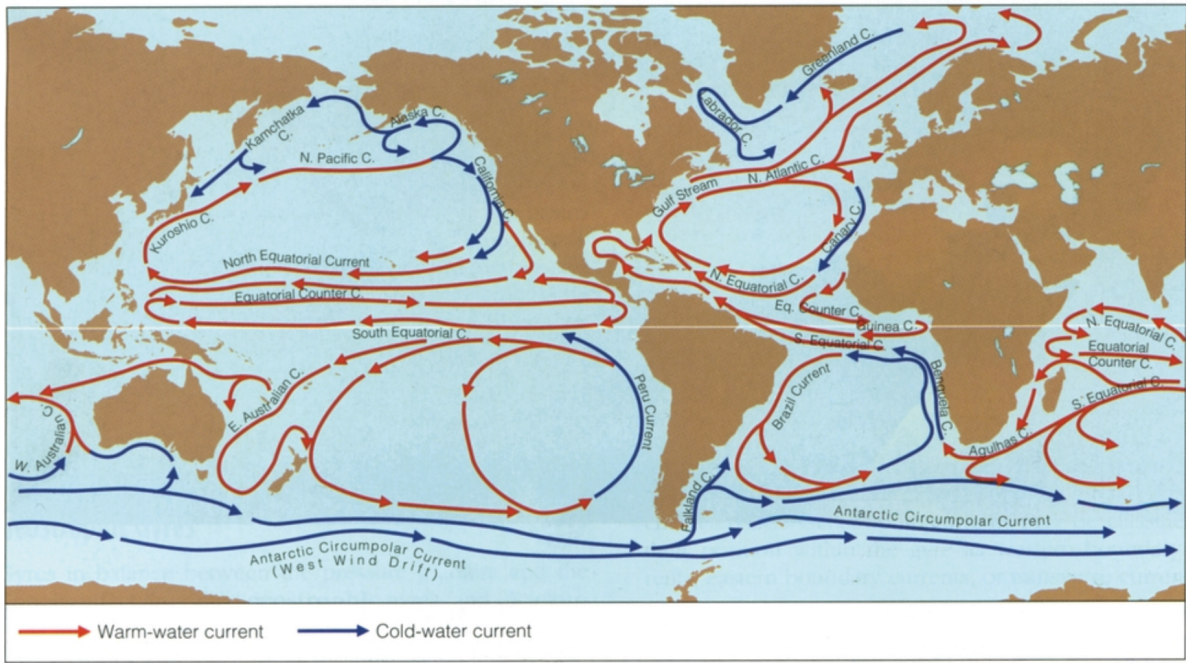

Figure: Surface circulation (Garrison, 2012).

Wind and buoyancy driven ocean circulation

- driven by wind stresses and pressure gradients
- surface and deep (= meridional overturning = thermohaline) circulation
- average horizontal velocities 0.01 - 0.1 m/s

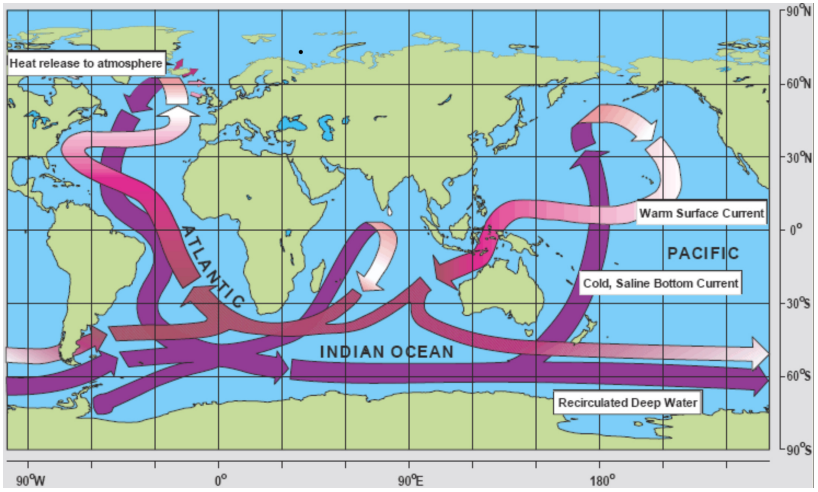

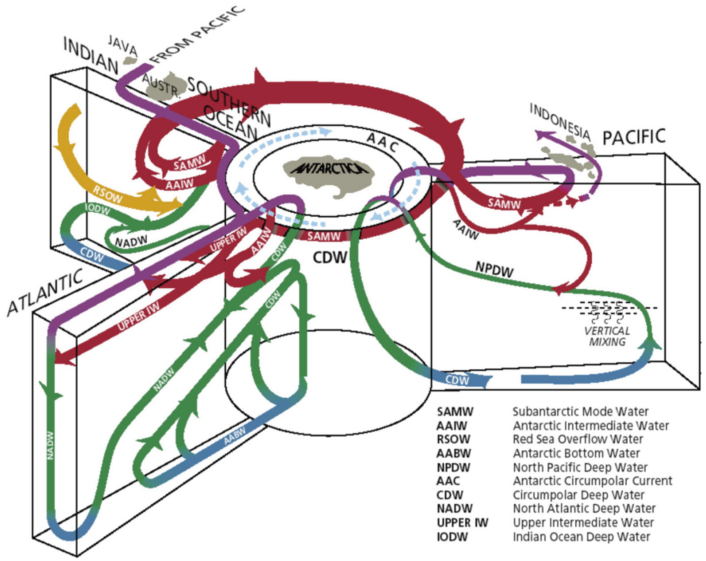

Figure: Deep circulation (Broecker et al., 1991; Schmitz Jr, 1996).

Previous seminars

- Baroclinic ocean model LSOMG (1.3. 2017)
- Elektromagnetická indukce v oceánech (25.4. 2017)
- Modelling of electromagnetic signatures of global ocean circulation: Physical approximations and numerical issues (27.2. 2019)
- EM induction in the Earth's Oceans II: Going big! (30. 10. 2019)

Today we focus on tides!

Tidal ocean circulation

- driven by gravitational forces of the Moon and the Sun

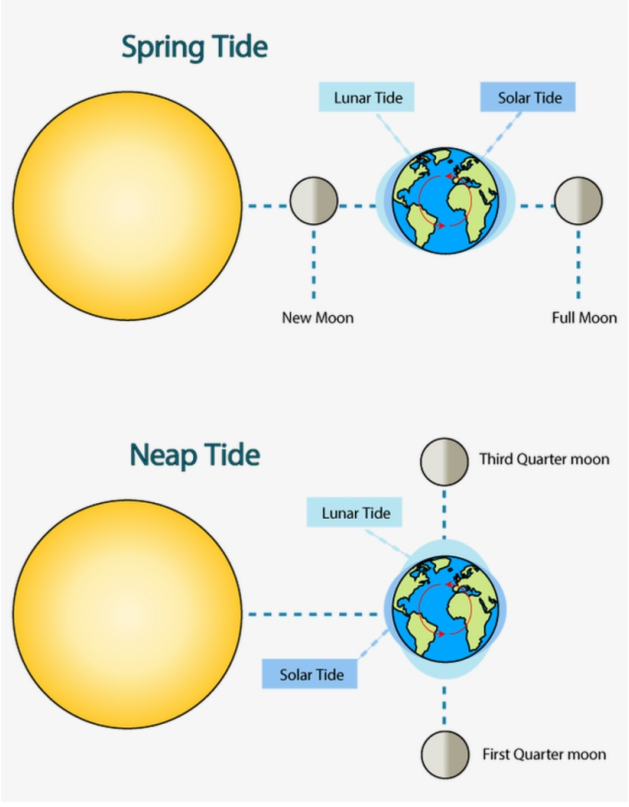

Figure: Tides caused by the Moon and the Sun (`https://www.clipart.email`).

Tidal ocean circulation

- distinct tidal frequencies $\Rightarrow$ frequency-domain modelling

Name of tide	Symb	Period	Freq. (s^{-1})- ω	K (m)	Ampl.
Semidiurnal Species					
Principal Lunar	M_2	12.421h	$1.40519 \cdot 10^{-4}$	0.242334	
Principal Solar	S_2	12.000h	$1.45444 \cdot 10^{-4}$	0.112841	
Elliptical Lunar	N_2	12.658h	$1.37880 \cdot 10^{-4}$	0.046398	
Declination Luni-Solar	K_2	11.967h	$1.45842 \cdot 10^{-4}$	0.030704	
Diurnal Species					
Declination Luni-Solar	K_1	23.934h	$0.72921 \cdot 10^{-4}$	0.141565	
Principal lunar	O_1	25.819h	$0.67598 \cdot 10^{-4}$	0.100574	
Principal solar	P_1	24.066h	$0.72523 \cdot 10^{-4}$	0.046843	
Elliptical lunar	Q_1	26.868h	$0.64959 \cdot 10^{-4}$	0.019256	
Long-Period Species					
Fortnightly Lunar	Mf	13.661d	$0.053234 \cdot 10^{-4}$	0.041742	
Monthly Lunar	Mm	27.555d	$0.026392 \cdot 10^{-4}$	0.022026	
Semiannual Solar	Ssa	182.621d	$0.0038921 \cdot 10^{-4}$	0.019446	

Figure: Parameters of major tidal constituents (Kowalik et al., 2006)

Tidal ocean circulation

- gravitational force is almost constant within the water column
  $\Rightarrow$ 2D flow

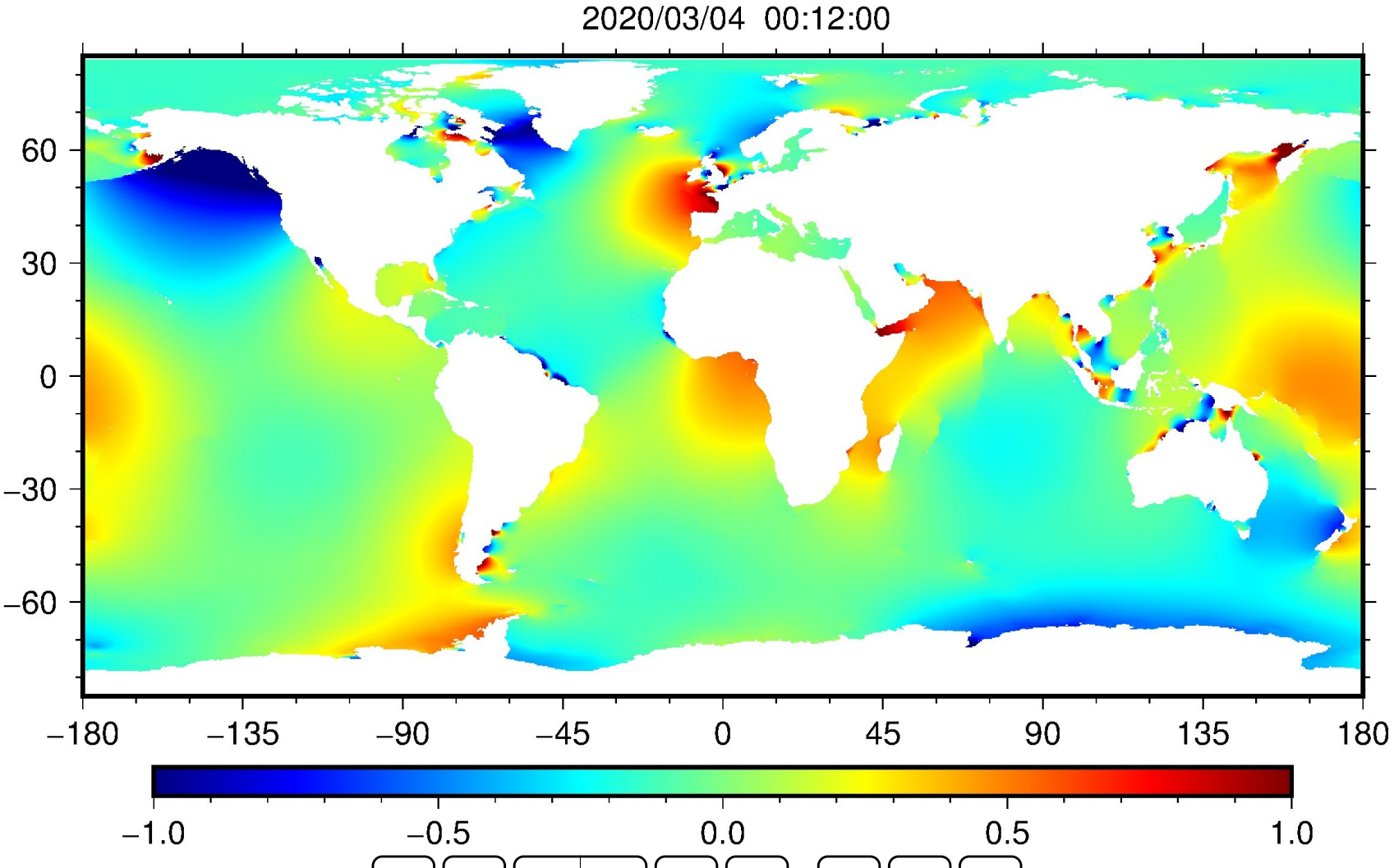

Why tides?

- sensitive to upper mantle structure
  - suitable frequencies
  - quasi-global coverage
  - non-trivial structure
- CHAMP (10 years) + Swarm (5 years) $\Rightarrow$
  - M_2 ($j \leq 28$)
  - N_2 ($j \leq 12$)
  - O_1 ($j \leq 12$)

  (Grayver and Olsen, 2019)
- 1 of 4 Swarm's key objectives: determine the 3D electrical conductivity of the mantle

Why tides?

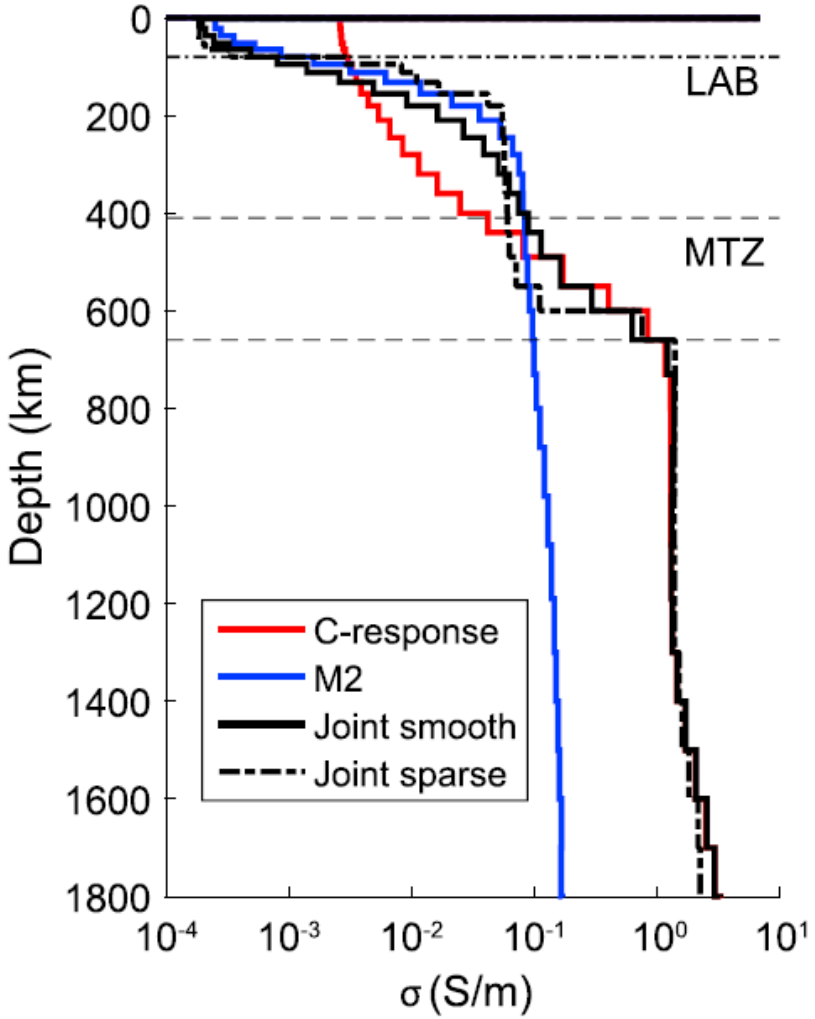

Figure: Combined inversion from magnetospheric and M_2 data (Grayver et al., 2017)

Current section

1 Introduction

2 Forward and inverse modelling

3 Numerical setup

4 Results

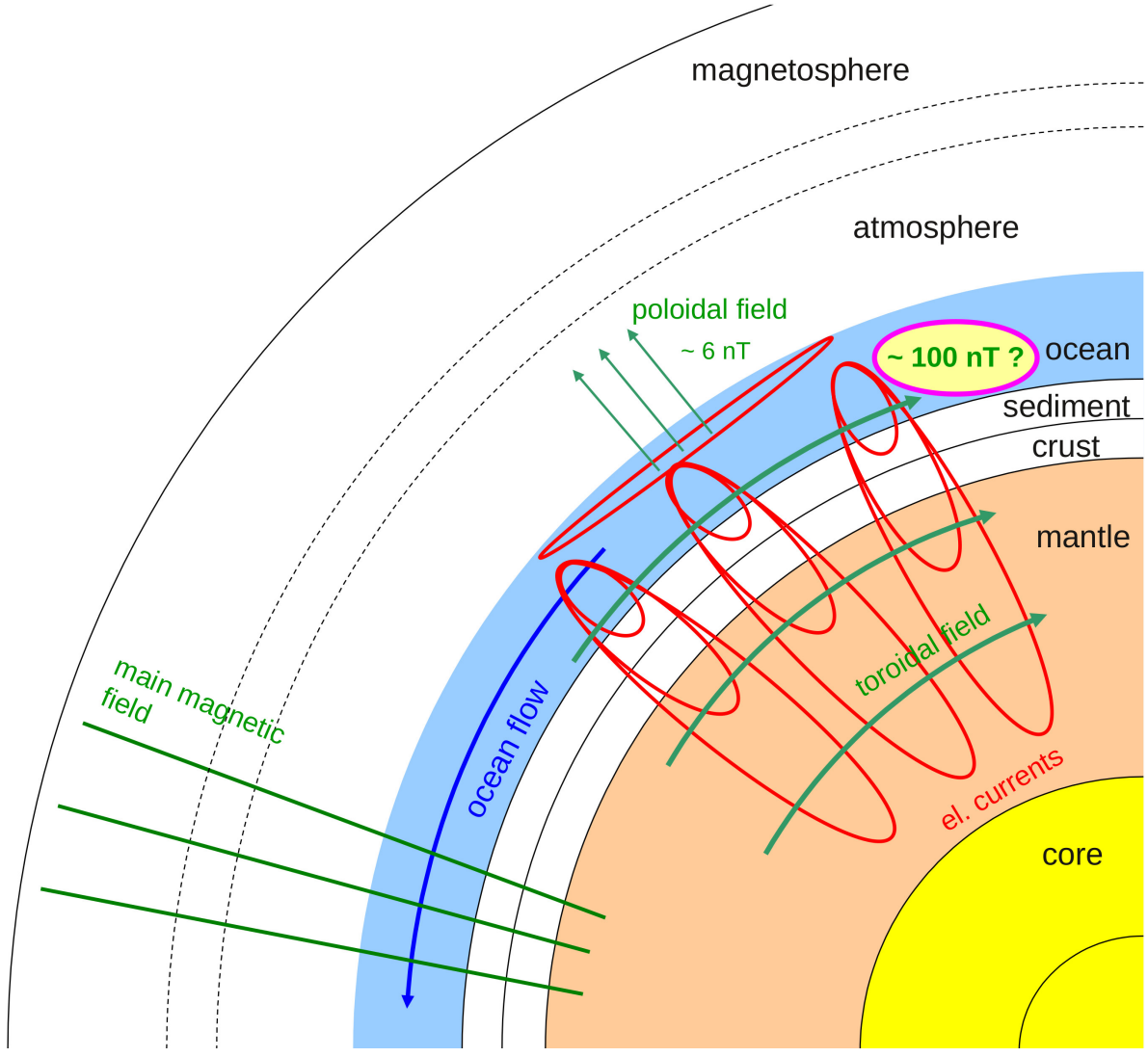

Figure: Illustration of EM induction in the Earth's oceans and mantle. Courtesy of Jan Dostál.

Governing equations

- quasi-static Maxwell equations suplemented by Ohm's law

$$\nabla \cdot \mathbf{B} = 0 \tag{1}$$

$$\nabla \times \mathbf{B} = \mu_0 \left(\mathbf{j} + \mathbf{j}^{\text{imp}} \right) \tag{2}$$

$$\nabla \times \mathbf{E} = -i\omega \mathbf{B} \tag{3}$$

$$\mathbf{j} = \sigma \mathbf{E} \tag{4}$$

- imposed electric field/currents

$$\mathbf{j}^{\text{imp}} = \sigma \mathbf{E}^{\text{imp}} = \sigma \left(\mathbf{u} \times \mathbf{B}_M \right)$$

- 3 assumptions:

$$\mathbf{B}_M = -\nabla V$$

$$\left| \frac{\partial \mathbf{B}_M}{\partial t} \right| \ll \left| \frac{\partial \mathbf{B}}{\partial t} \right|$$

$$|\mathbf{B}| \ll |\mathbf{B}_M|$$

ElmgFD

- solves the EM induction equation in the frequency domain

$$\nabla \times \left(\frac{1}{\sigma} \nabla \times \mathbf{B} \right) - i\omega\mu_0 \mathbf{B} = \mu_0 \nabla \times \mathbf{E}^{\text{imp}}$$

- complex vector spherical harmonic functions in angular coordinates
  - separation of poloidal and toroidal magnetic field modes
  - high contrast of electrical conductivity $\Rightarrow$ Gibbs phenomenon
  - difficult to locally refine the grid
- piecewise-linear 1-D finite elements in radial coordinate
- divergence-free constraint enforced by means of Lagrange multipliers
- solves a system of linear equations with block-tridiagonal matrix using iterative solver with a 1D preconditioner

Inversion

- model parameters m_i, $i \in \{1, \ldots, M\}$

$$\log_{10}\left[\sigma(\mathbf{m};\mathbf{r})/\sigma_0\right] = \sum_{i=1}^{M} m_i \zeta_i(\mathbf{r}) + \sum_{i=M+1}^{M_0} m_i^0 \zeta_i(\mathbf{r})$$

  - $\zeta_i(\mathbf{r})$ are picewise-constant functions
  - model parameters m_i^0 have fixed values (regions below continents)
- minimize penalty function (Velímský, 2013)

$$\widetilde{\mathbf{m}}(\lambda) = \arg\min_{\mathbf{m}\in R^M} \left[\chi^2(\mathbf{m}) + \lambda R(\mathbf{m})\right]$$

$$\chi^2(\mathbf{m}) = \sum_l \sum_{jm} \frac{(2j+1)(j+1)}{8\pi} \left| \frac{G_{jm}^{(\mathrm{i})}(\mathbf{m};\omega_l) - G_{jm}^{(\mathrm{i,obs})}(\omega_l)}{\delta_{jm}^{(\mathrm{i})}(\omega_l)} \right|^2$$

Adjoint approach

We follow Maksimov and Velímský (2017).

Forward problem for ω_l:

$$\nabla \times [\rho(\mathbf{r}) \nabla \times \mathbf{B}(\mathbf{r}; \omega_l)] - \mathrm{i}\omega_l \mu_0 \mathbf{B}(\mathbf{r}; \omega_l) = \mu_0 \nabla \times (\mathbf{v} \times \mathbf{B}_0)$$

Adjoint problem for ω_l:

$$\nabla \times \left[\rho(\mathbf{r}) \nabla \times \hat{\mathbf{B}}(\mathbf{r}; \omega_l)\right] + \mathrm{i}\omega_l \mu_0 \hat{\mathbf{B}}(\mathbf{r}; \omega_l) = \mathbf{0}$$

or

$$\nabla \times \left[\rho(\mathbf{r}) \nabla \times \overline{\hat{\mathbf{B}}}(\mathbf{r}; \omega_l)\right] - \mathrm{i}\omega_l \mu_0 \overline{\hat{\mathbf{B}}}(\mathbf{r}; \omega_l) = \mathbf{0}$$

Adjoint approach

Adjoint source for ω_l:

$$\hat{G}^{(\mathrm{e,obs})}_{jm}(\omega_l) = +\mathrm{i}\,\frac{j+1}{2}\,\frac{G^{(\mathrm{i})}_{jm}(\mathbf{m};\omega_l) - G^{(\mathrm{i,obs})}_{jm}(\omega_l)}{\left[\delta^{(\mathrm{i})}_{jm}(\omega_l)\right]^2}$$

or

$$\overline{\hat{G}^{(\mathrm{e,obs})}_{jm}}(\omega_l) = -\mathrm{i}\,\frac{j+1}{2}\,\frac{\overline{G^{(\mathrm{i})}_{jm}}(\mathbf{m};\omega_l) - \overline{G^{(\mathrm{i,obs})}_{jm}}(\omega_l)}{\left[\delta^{(\mathrm{i})}_{jm}(\omega_l)\right]^2}$$

Adjoint approach

Derivative of misfit with respect to m_α:

$$\mathrm{D}_\alpha \chi^2(\mathbf{m}) = \frac{2}{4\pi\, a^3\, \mu_0} \mathrm{Re}\left(\sum_l \frac{1}{\omega_l} \int_G I \,\mathrm{d}V \right),$$

$$I = \mathrm{D}_\alpha \rho(\mathbf{m};\mathbf{r})\, \nabla \times \mathbf{B}(\mathbf{m};\mathbf{r};\omega_l) \cdot \nabla \times \overline{\hat{\mathbf{B}}}(\mathbf{m};\mathbf{r};\omega_l),$$

where

$$D_\alpha \rho = -(\ln 10)\rho(\mathbf{m};\mathbf{r})\zeta_\alpha(\mathbf{r})$$

Current section

1 Introduction

2 Forward and inverse modelling

3 Numerical setup

4 Results

Forcing

- 2D TPXO9 M_2 tidal velocities
  - $(1/30)^\circ \times (1/30)^\circ$
  - bilinearly interpolated to ElmgFD grid

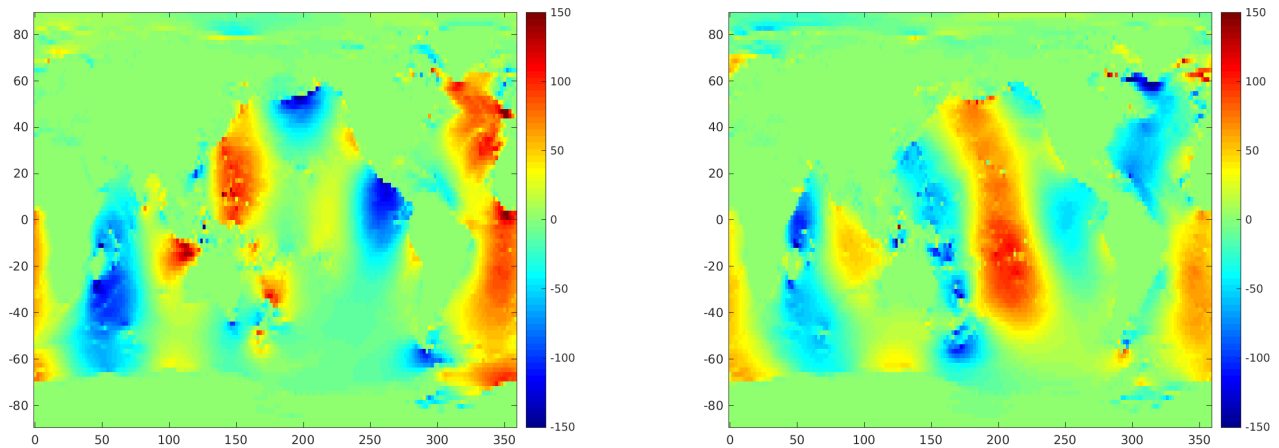

Figure: Real (left) and imaginary (right) parts of zonal barotropic transports [m^2/s].

- 12th generation of the International Geomagnetic Reference Field (IGRF–12, Thébault et al., 2015) $\mathbf{B}_M$
  - constant with depth

Surface conductivity, ocean σ_{oc}

- mean σ_{oc} is 3.31 ± 0.23 S/m (3.2 S/m in our benchmarks)

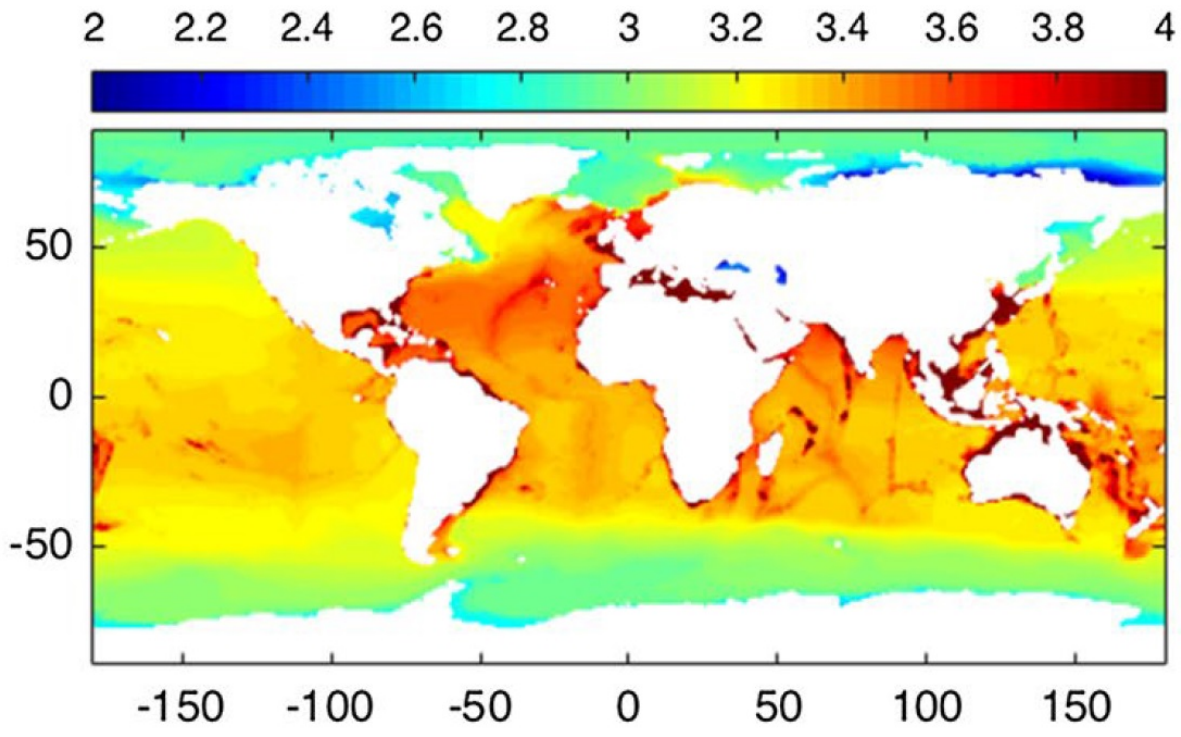

Figure: Vertically averaged conductivity of the global ocean (Tyler et al., 2017).

Surface conductivity, ocean σ_{oc}

- we use σ_{oc} of Tyler et al. (2017)
  - annual means $\Rightarrow$ constant in time
  - depends on S, p and T $\Rightarrow$ spatially variable
  - 102 layers layers
  - from surface down to 5500 m

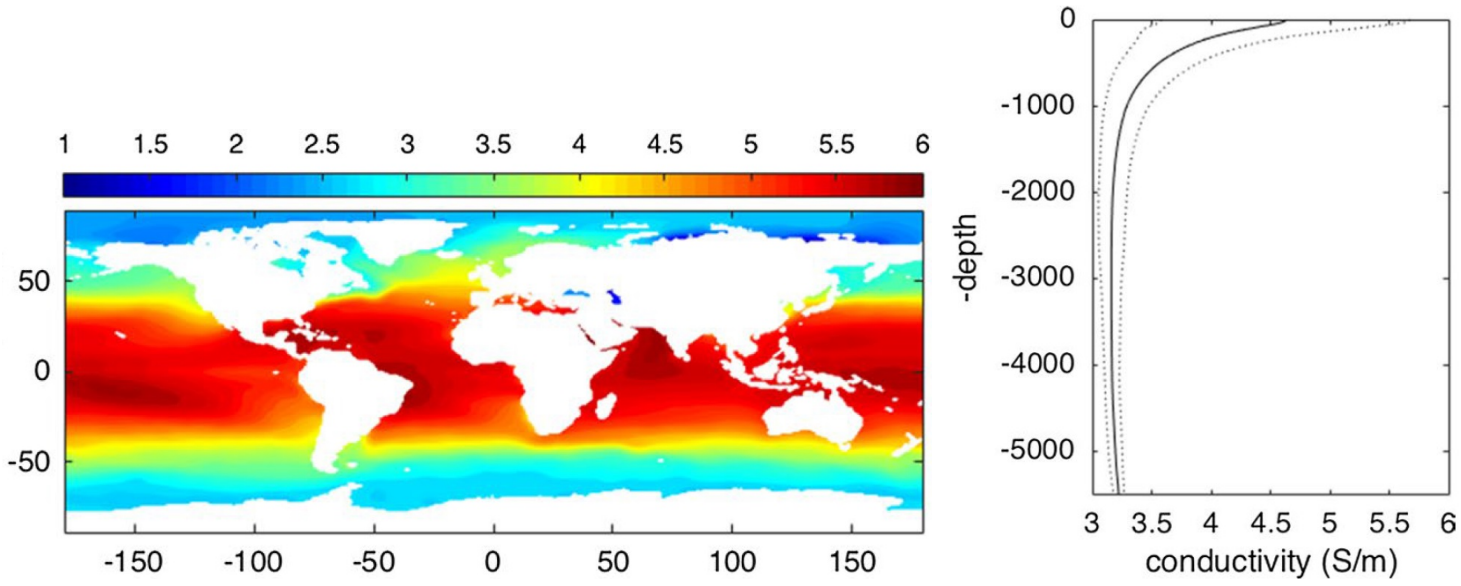

Figure: Surface conductivity (left) and globally averaged ocean conductivity profile (right) (Tyler et al., 2017).

Surface conductivity, sediments

Type	σ [S/m]
oceanic s. A	0.8
oceanic s. B	0.02
coastal s.	0.5
continental s.	0.03
igneous	0.001

Table: Conductivity of igneous rocks and sediments.

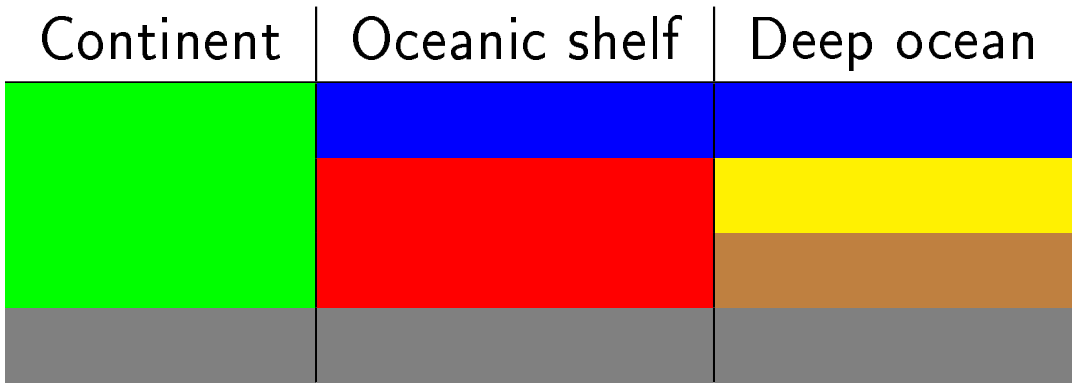

Table: Schematic layout of conductivity layers below continents, oceanic shelfs and deep ocean.

3D conductivity of upper mantle, model WINTERC-e

Original model (Fullea et al., 2019):

- 0-402 km
- 201 layers, each 2 km thick
- irregular grid

We use averaged version on 90×180 Gauss-Legendre grid:

- vertical averaging: 10 layers
- horizontal averaging: 4-7 neighbouring data points

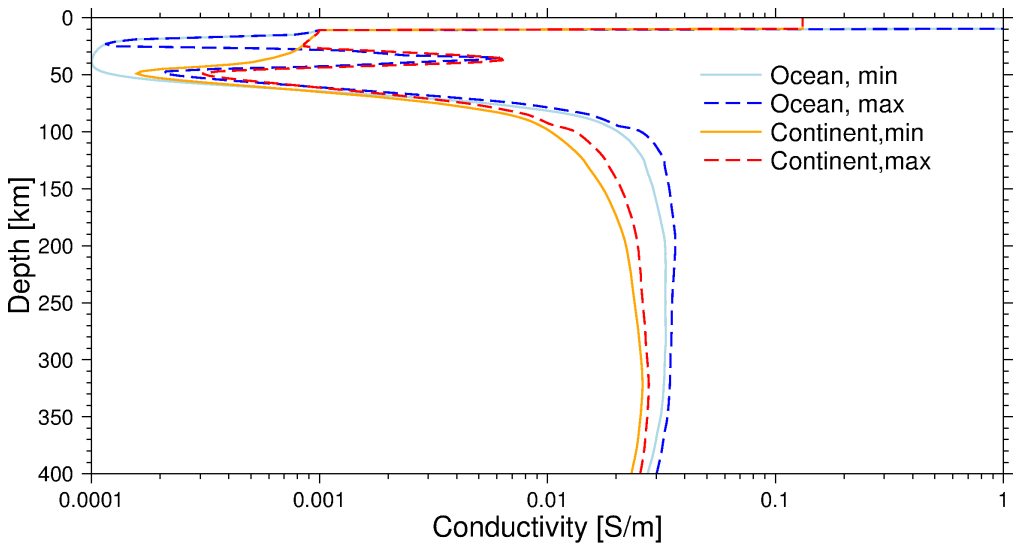

Figure: 1D profiles.

1D conductivity model of lower mantle and core

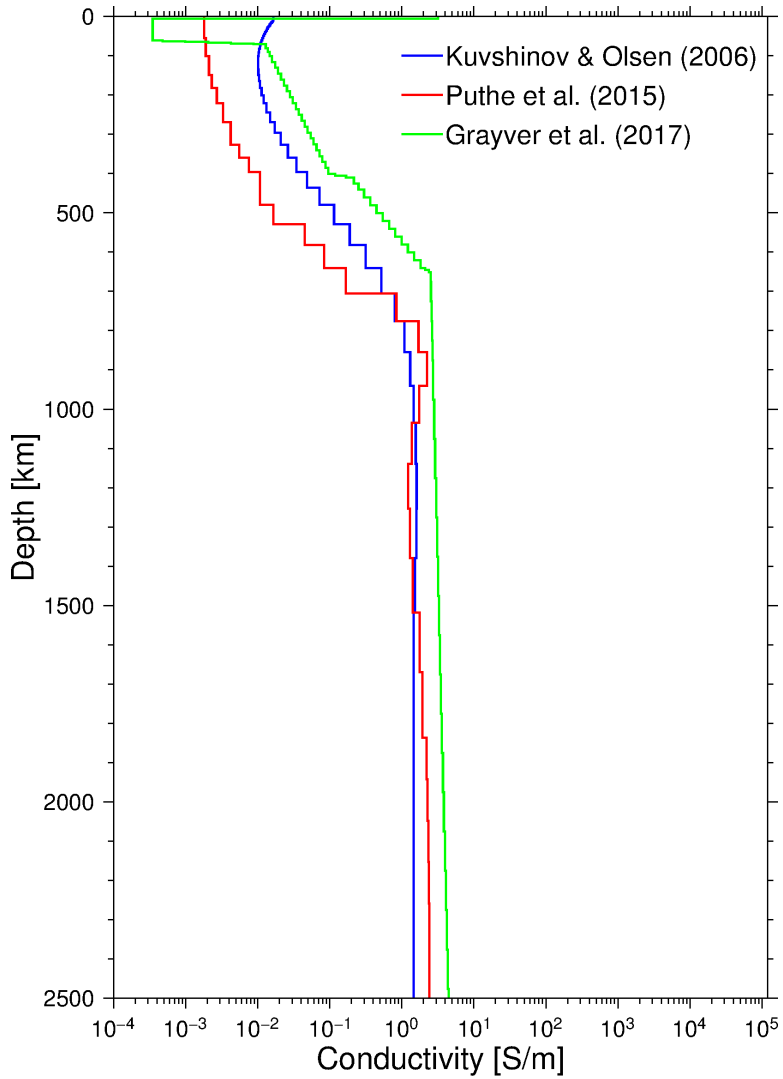

Figure: 1D conductivity models.

ElmgFD configuration

- spherical-harmonic truncation degree $j_{max} = 60$
- 90×180 ($2^\circ \times 2^\circ$) Gauss-Legendre grid
- total of 165 layers
  - 3D ocean layers: 102
  - 3D upper-mantle layers: 21
  - 1D core and lower-mantle layers: 43
- inverse problem
  - $6^\circ \times 6^\circ$ grid cells
  - 15 210 model parameters
  - 13 layers

Current section

1 Introduction

2 Forward and inverse modelling

3 Numerical setup

4 Results

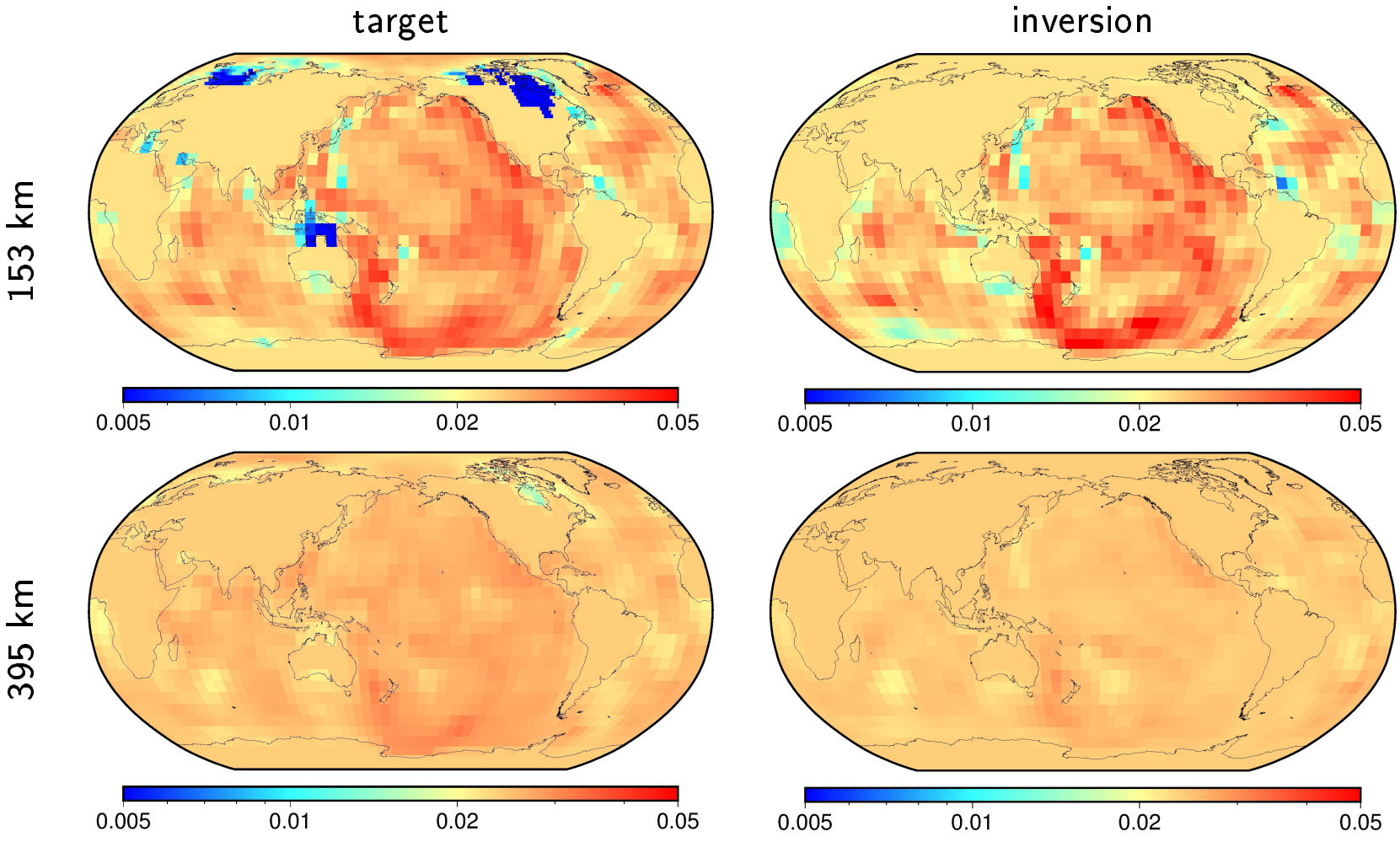

Figure: Target and inverted conductivity [S/m] in the depth of 153 km and 395 km. Internal coefficients on surface. No regularization.

OIMF in the outer space

$$\nabla \times \mathbf{B} = 0 \quad \Rightarrow \quad \mathbf{B} = -\nabla U,$$
$$\nabla \cdot \mathbf{B} = 0 \quad \Rightarrow \quad \Delta U = 0, \qquad \lim_{r \to \infty} U = 0.$$

$$U(\mathbf{r}, t) = a \sum_{j=1}^{\infty} \sum_{m=-j}^{j} G_{jm}^{(i)}(t) \left(\frac{a}{r}\right)^{j+1} Y_{jm}(\vartheta, \varphi)$$

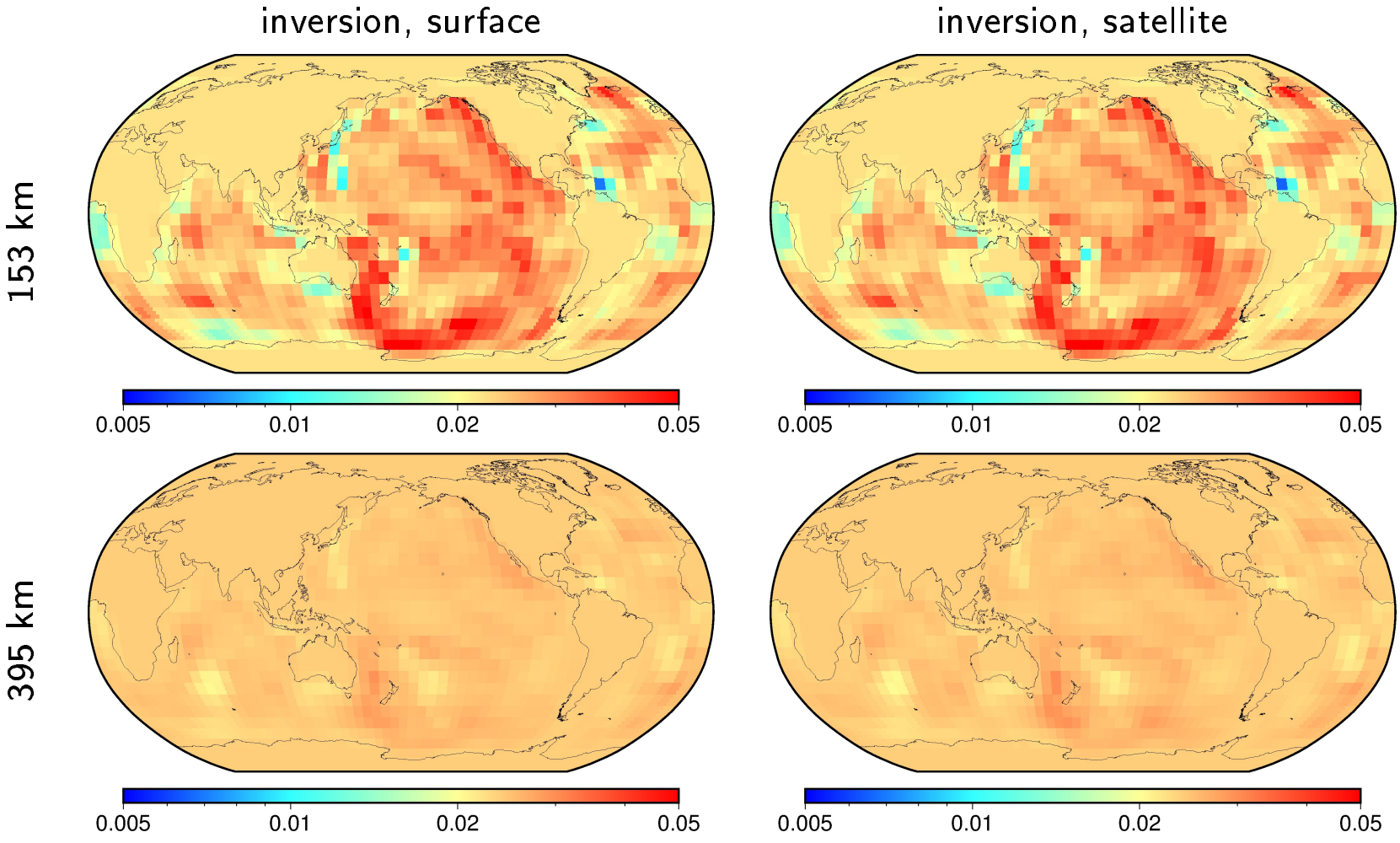

Figure: Effect of height where internal coefficients are "measured" on the conductivity [S/m] determined by inversion. No regularization.

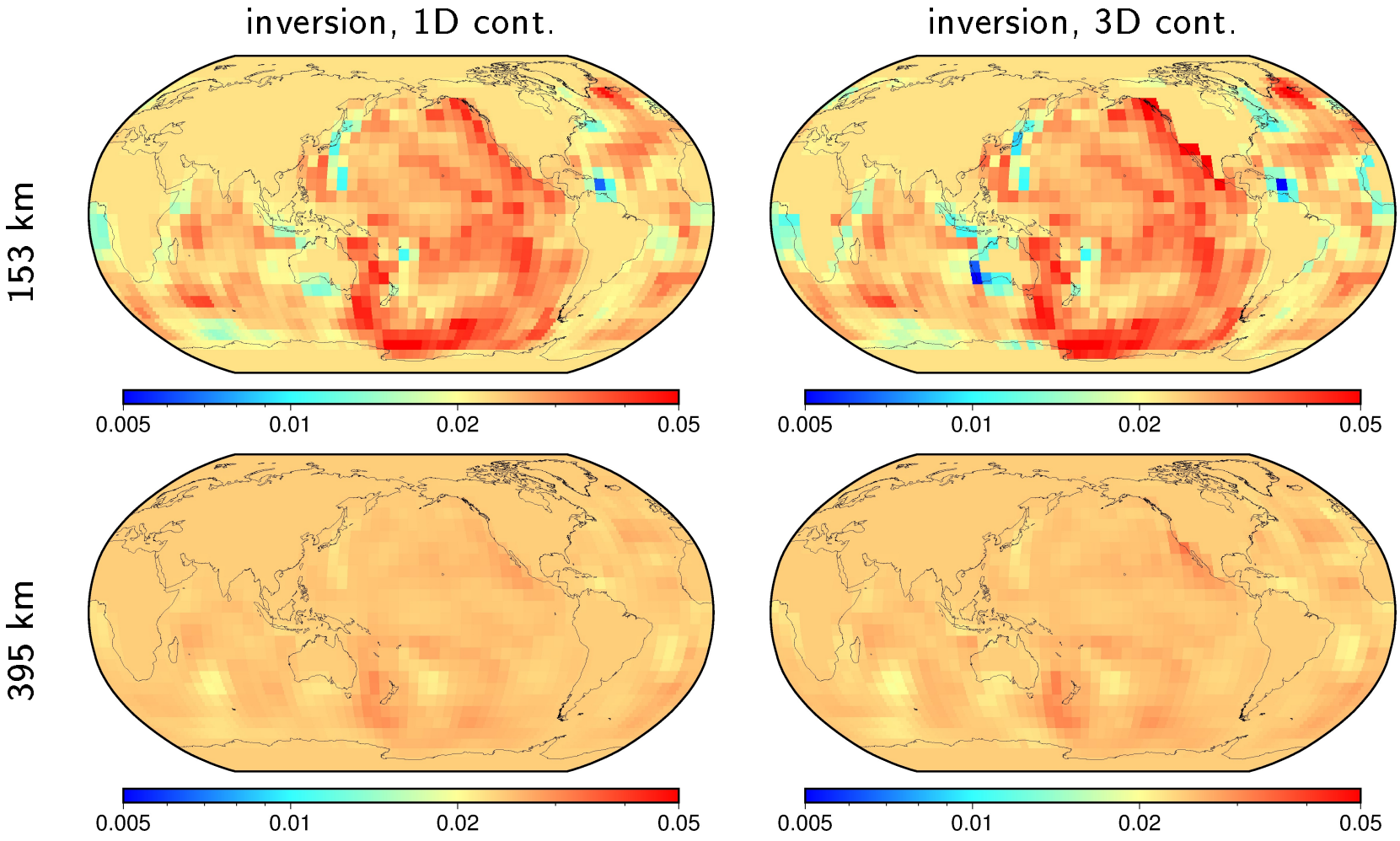

Figure: Effect of 1D/3D continental conductivity in the generation of synthetic internal coefficients on the conductivity [S/m] determined by inversion. No regularization.

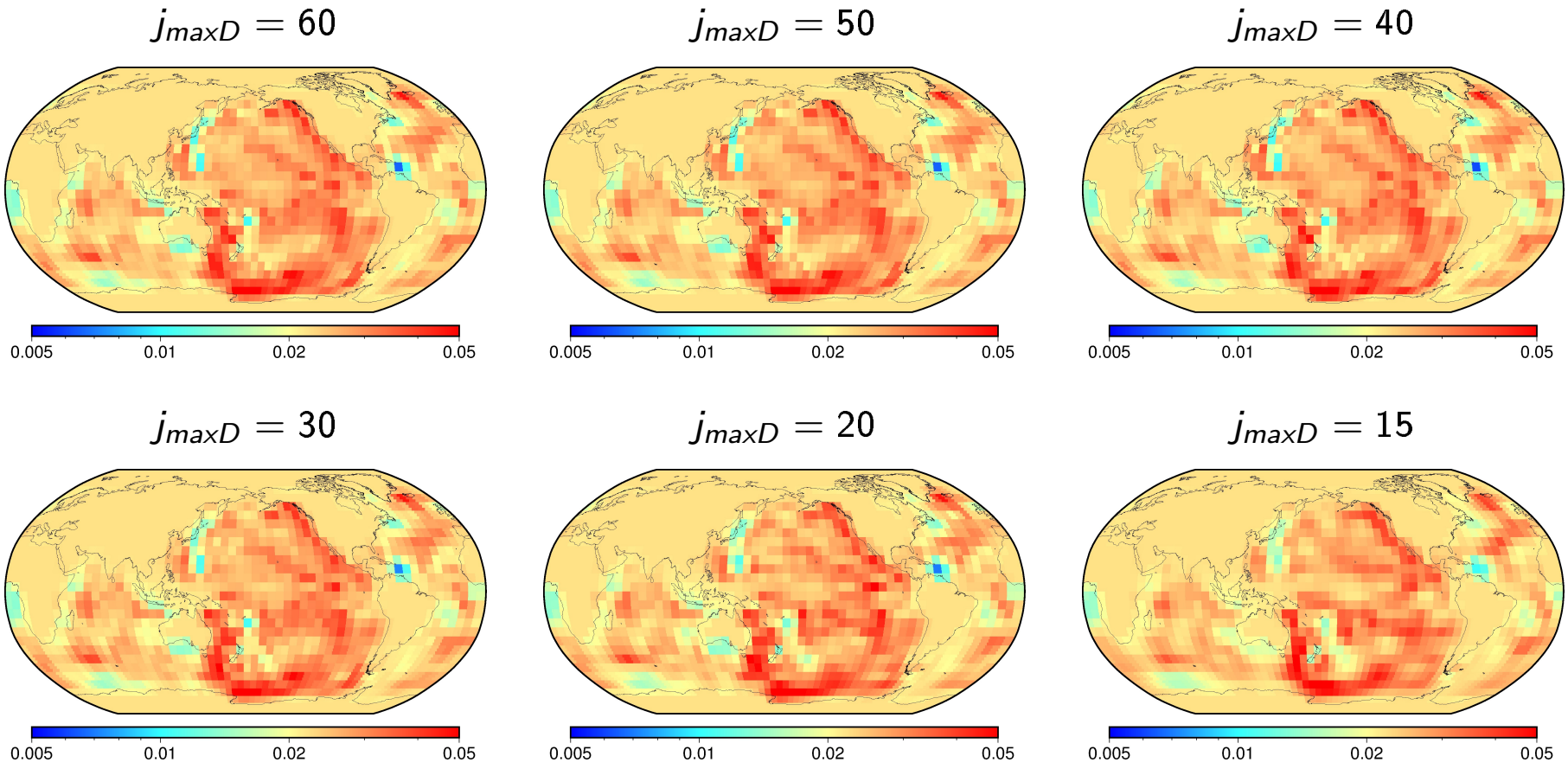

Figure: Effect of maximum degree j_{maxD} of synthetic internal coefficients on the conductivity [S/m] in the depth of 153 km. No regularization.

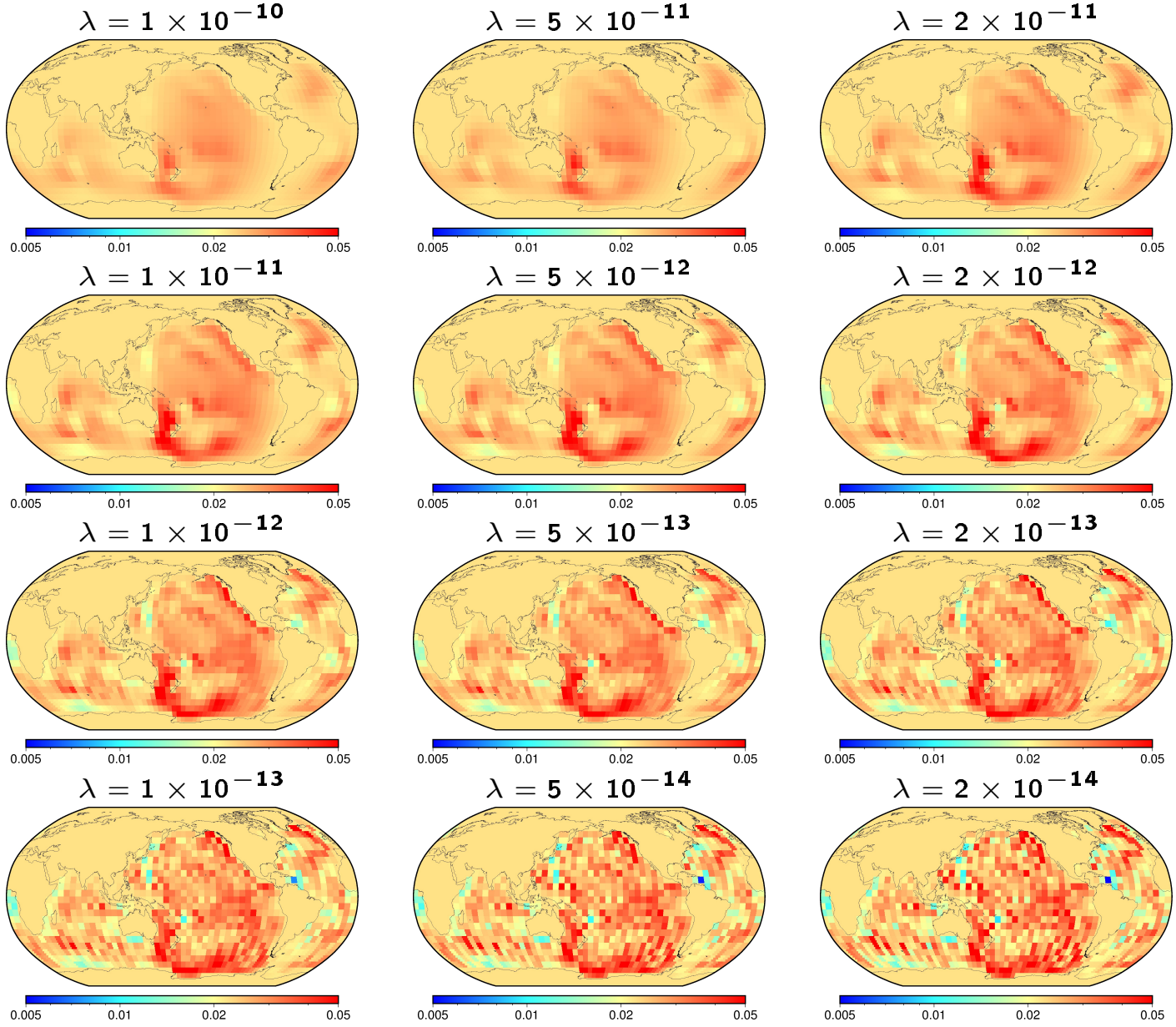

Figure: Conductivity [S/m] in layer 56 in the presence of 5% noise for $j > 30$. Regularization: Horizontal derivative of logarithm of rezistivity in all inspected layers.

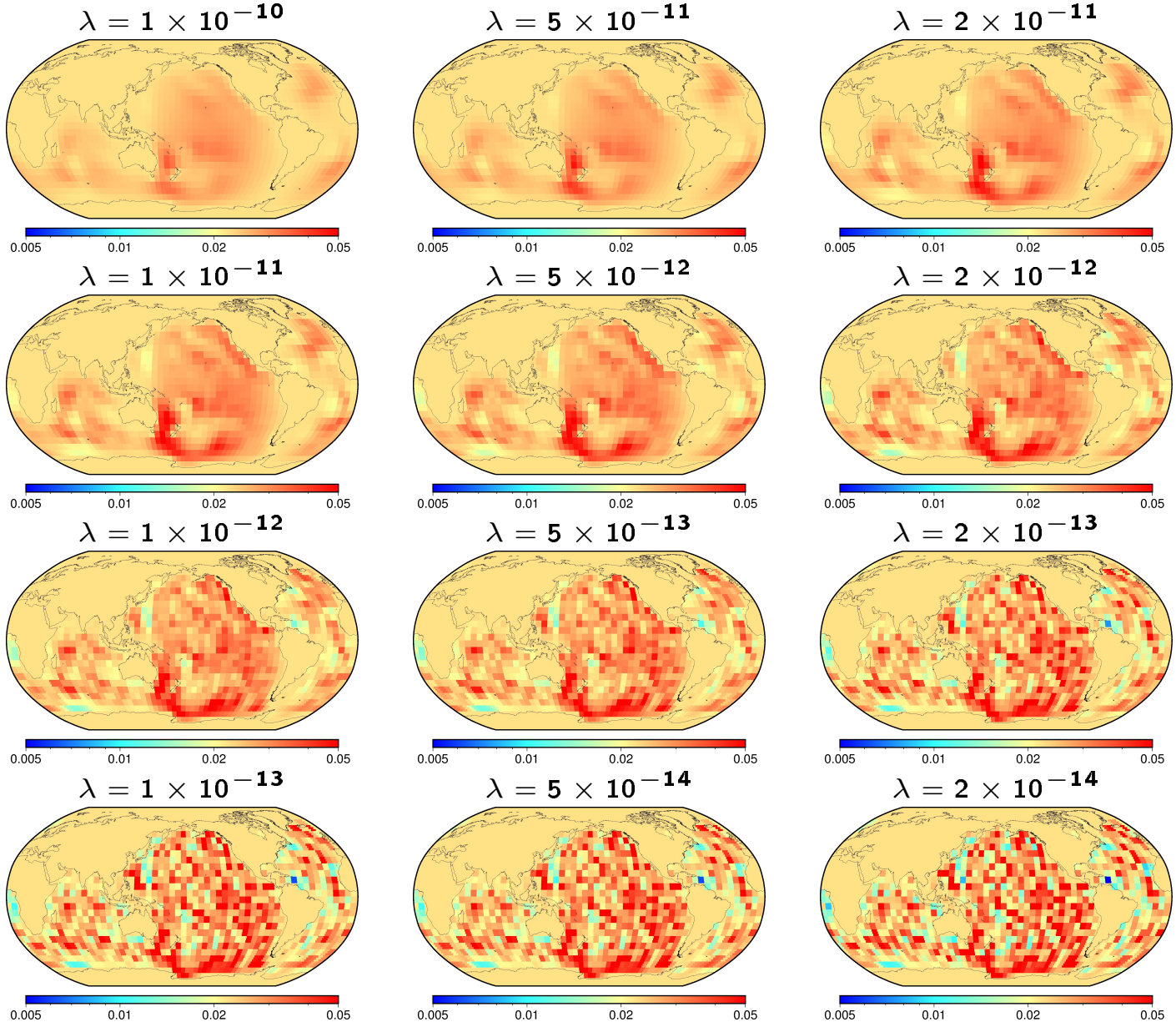

Figure: Conductivity [S/m] in layer 56 in the presence of 5% noise for $j > 20$. Regularization: Horizontal derivative of logarithm of rezistivity in all inspected layers.

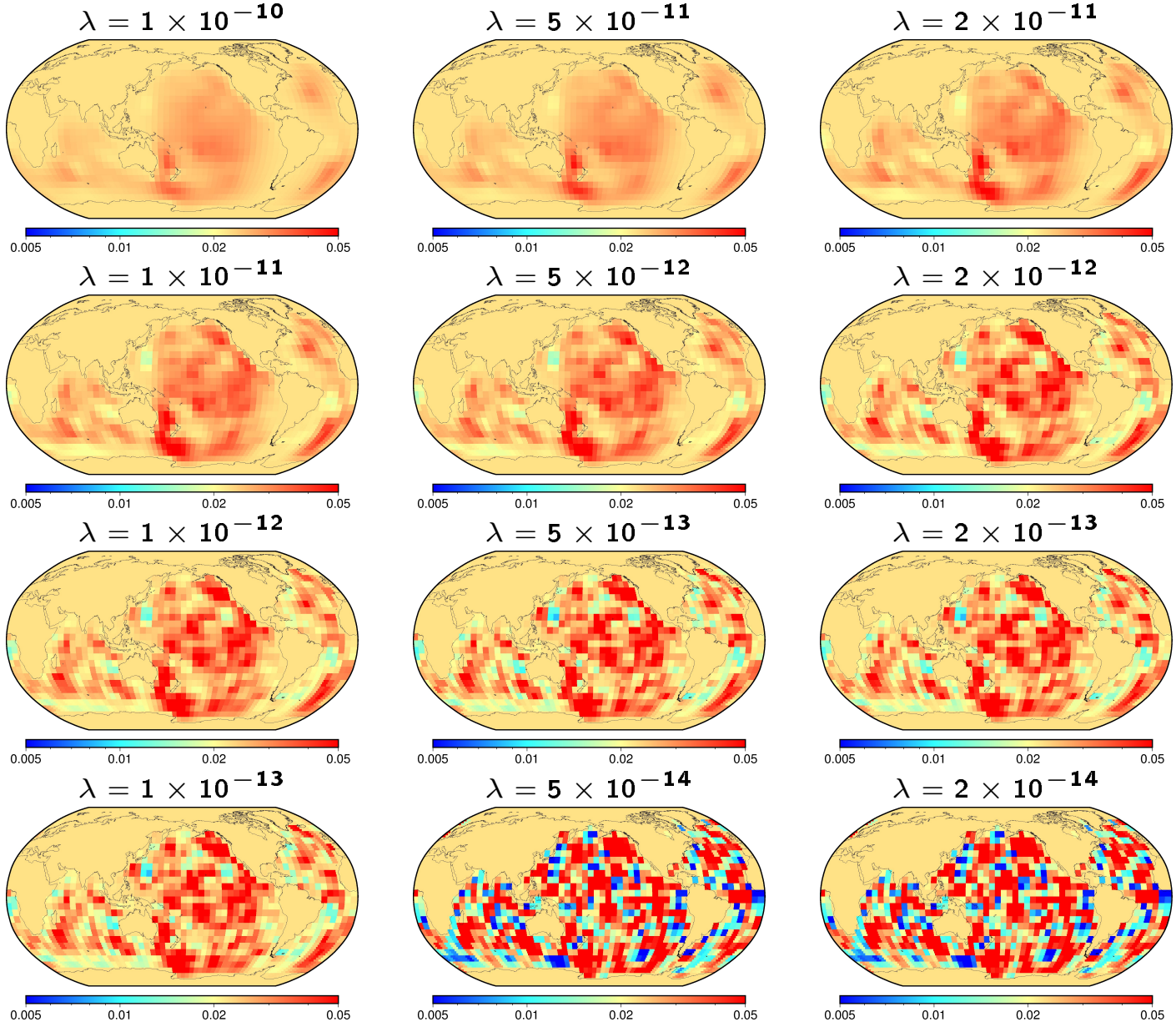

Figure: Conductivity [S/m] in layer 56 in the presence of 5% noise for $j > 10$. Regularization: Horizontal derivative of logarithm of rezistivity in all inspected layers.

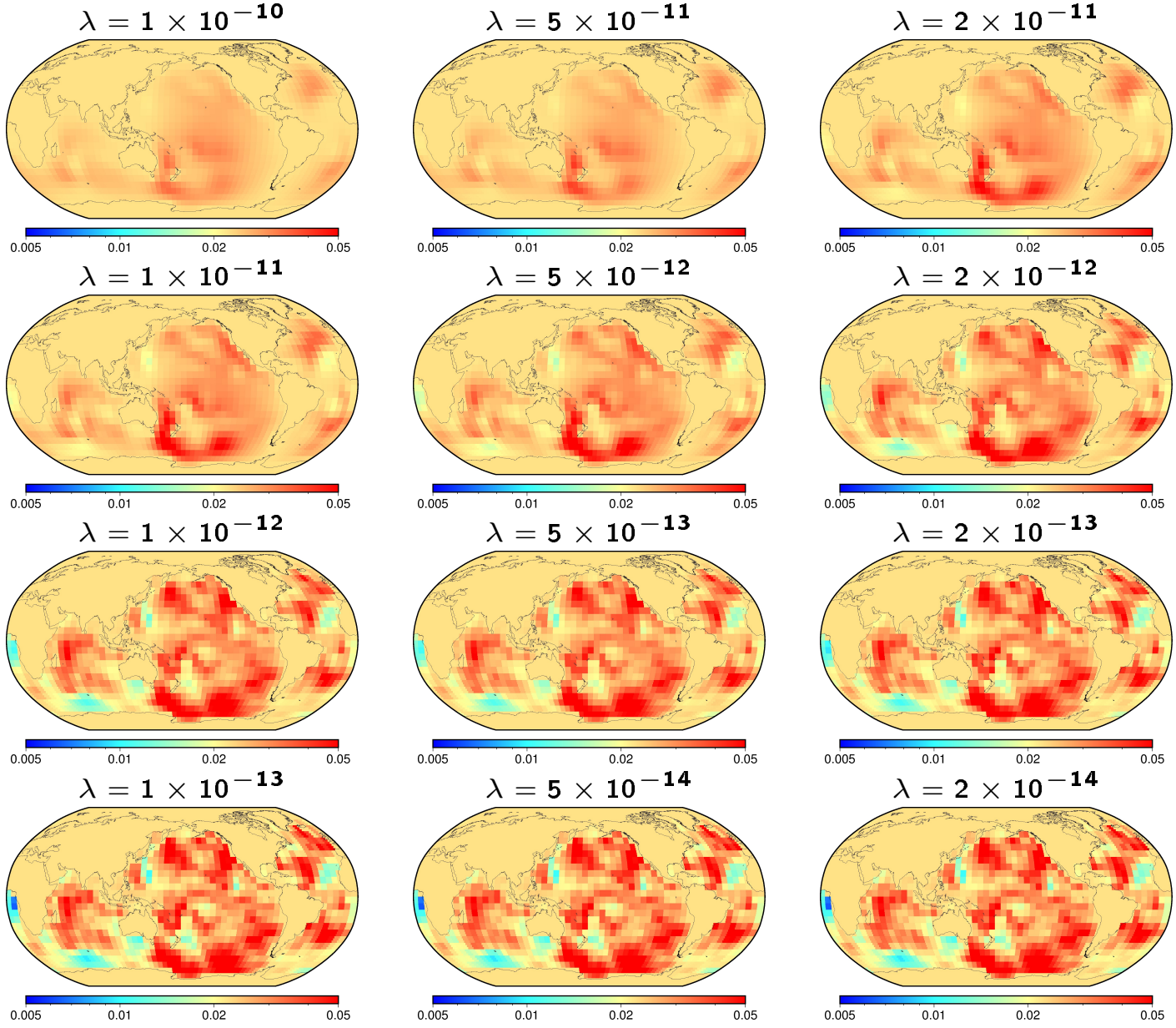

Figure: Conductivity [S/m] in layer 56 in the presence of 1% noise for all j. Regularization: Horizontal derivative of logarithm of rezistivity in all inspected layers.

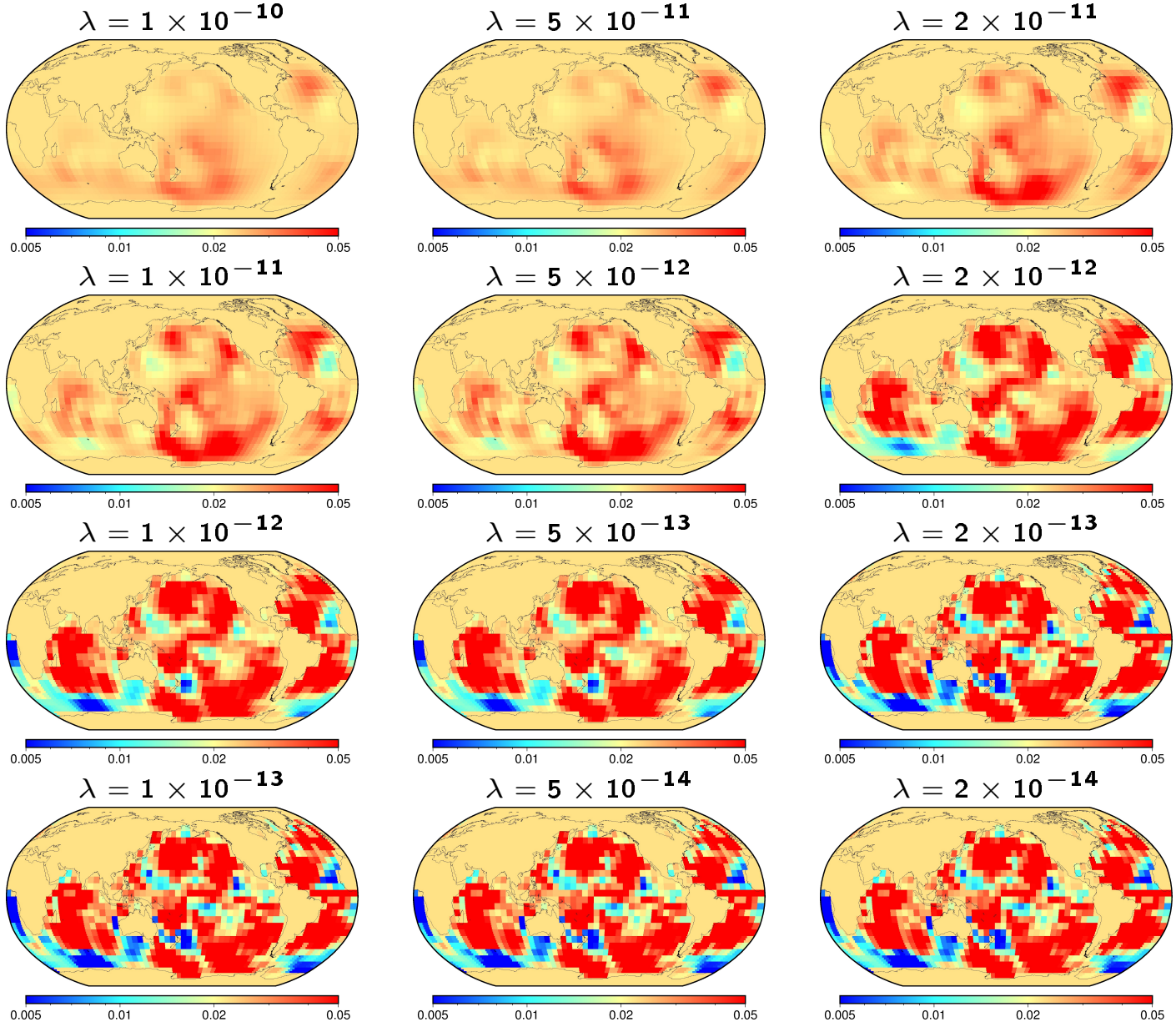

Figure: Conductivity [S/m] in layer 56 in the presence of 3% noise for all j. Regularization: Horizontal derivative of logarithm of rezistivity in all inspected layers.

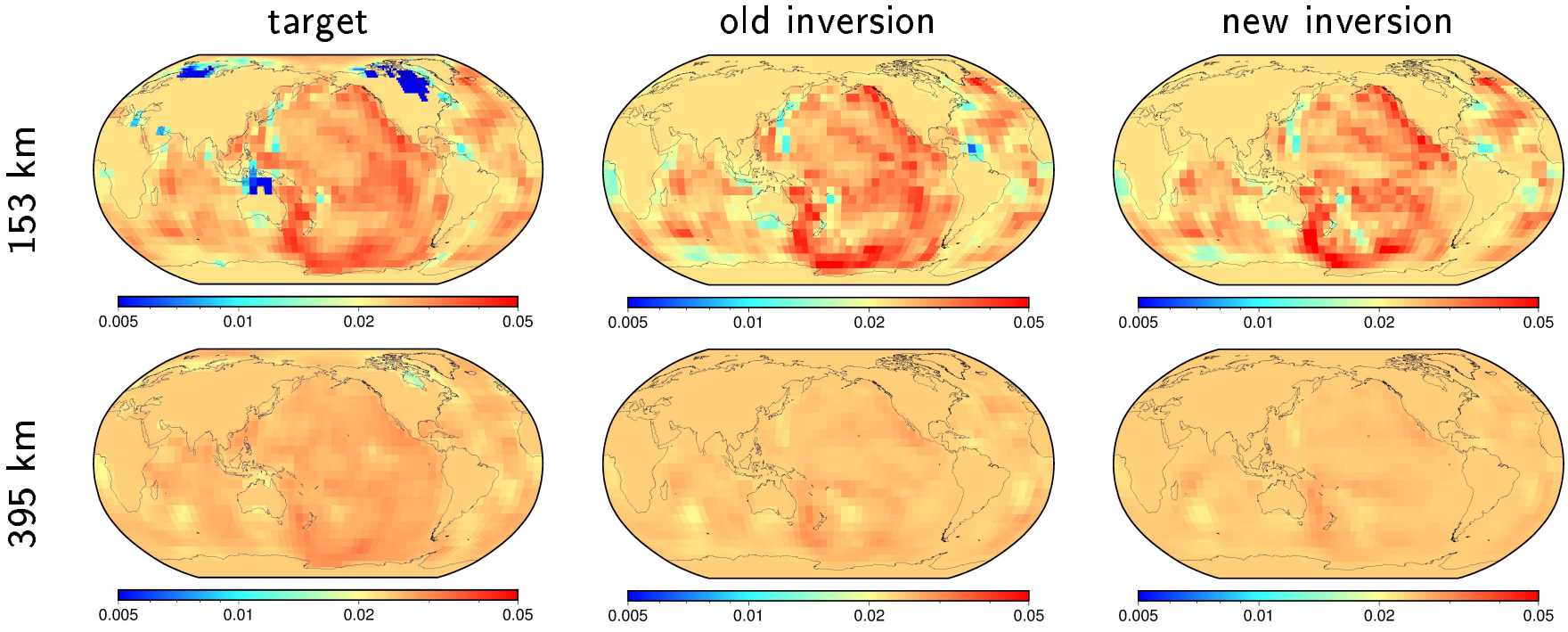

Figure: Target, old and new inverted conductivity [S/m] in the depth of 153 km and 395 km. Internal coefficients at satellite height. No regularization.

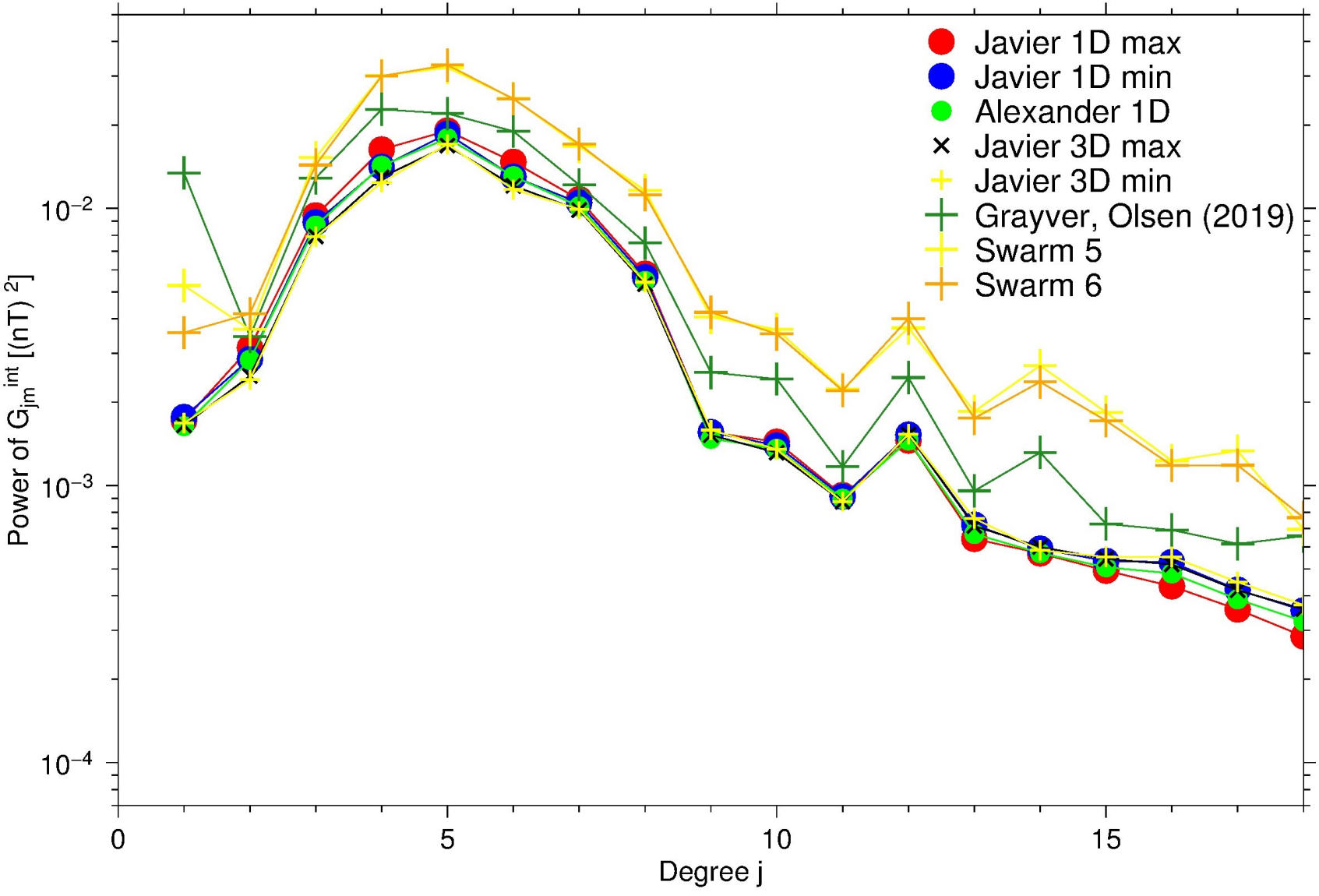

Figure: Power spectra from data and our numerical simulations with 3D forcing.

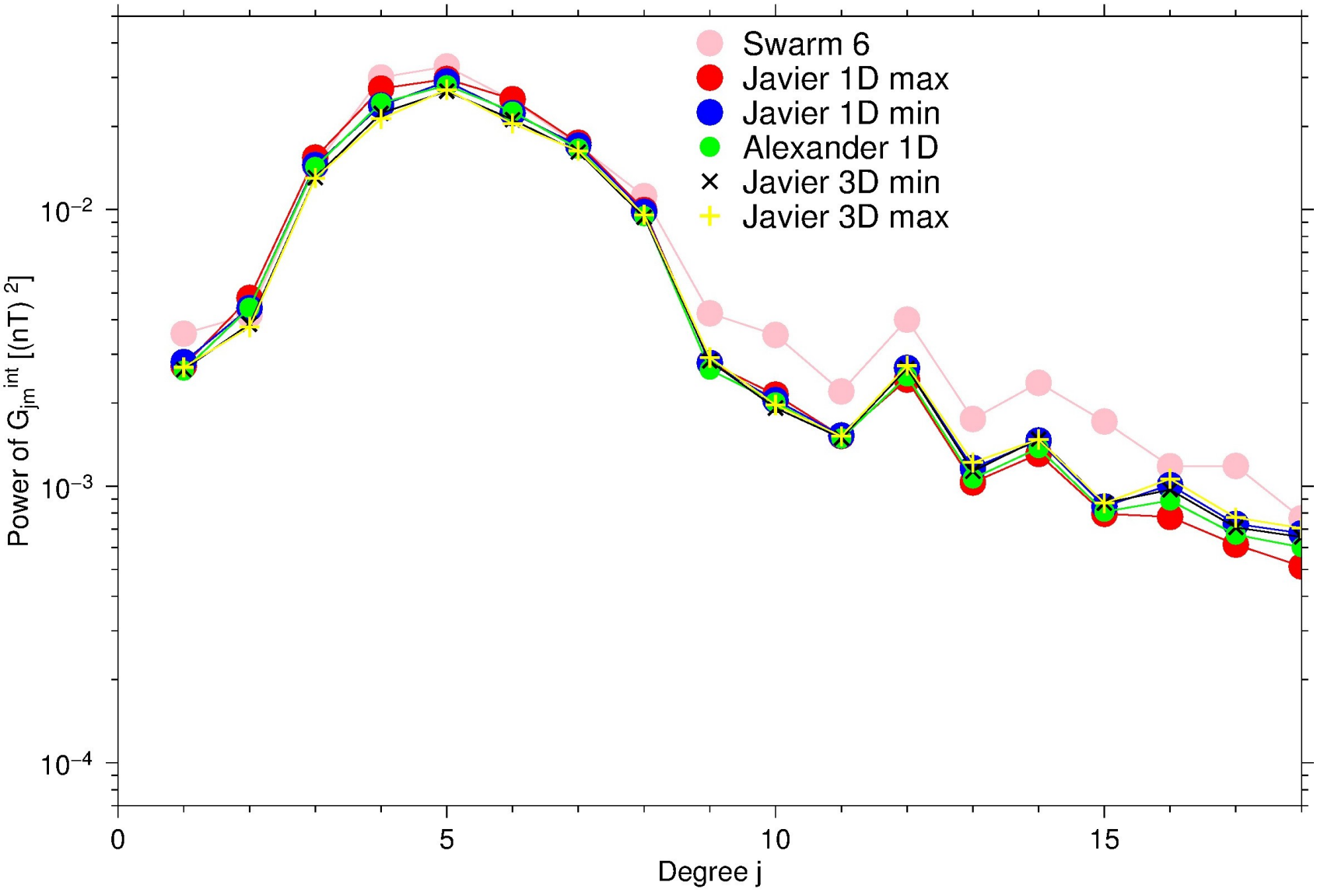

Figure: Power spectra from data and our numerical simulations with 2D forcing.

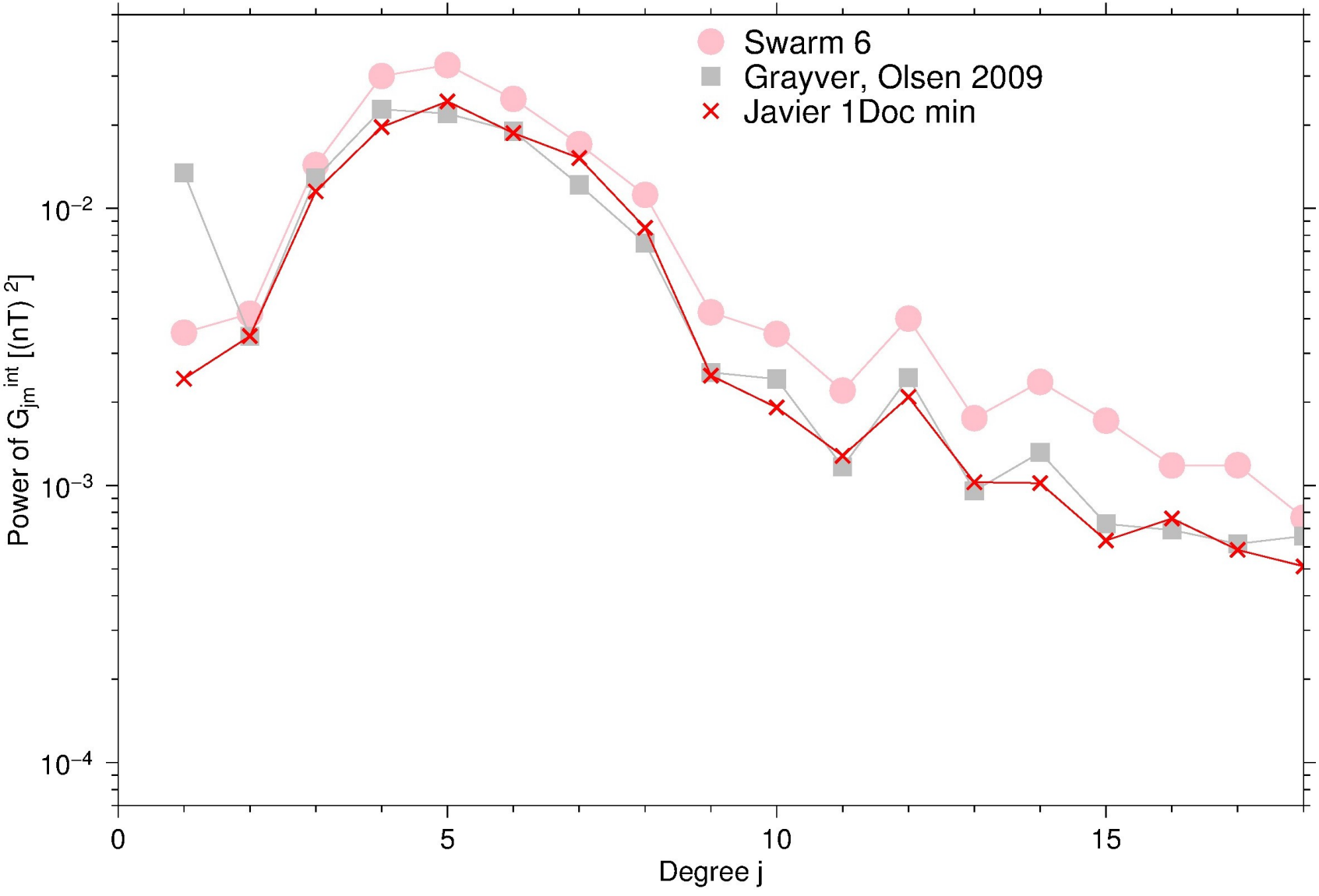

Figure: Power spectra from data and our new numerical simulations with 3D forcing.

Summary

- we established a framework for the 3D inversion of tidally induced magnetic field
- synthetic tests are promising for the inversion of real data ...
- ... but the discrepancies between available data sets are discouraging

Broecker, W.S., et al., 1991. The great ocean conveyor. Oceanography 4, 79–89.

Fullea, J., Lebedev, S., Martinec, Z., Celli, N.L., 2019. WINTERC-grav: mapping the upper mantle thermochemical heterogeneity from coupled geophysical-petrological inversion of seismic waveforms. Geophys. J. Int. , under review.

Garrison, T.S., 2012. Essentials of oceanography. Cengage Learning.

Grayver, A., Munch, F., Kuvshinov, A., Khan, A., Sabaka, T., Tøffner-Clausen, L., 2017. Joint inversion of satellite-detected tidal and magnetospheric signals constrains electrical conductivity and water content of the upper mantle and transition zone. Geophys. Res. Lett. 44, 6074–6081.

Grayver, A.V., Olsen, N., 2019. The magnetic signatures of the m 2, n 2, and o 1 oceanic tides observed in swarm and champ satellite magnetic data. Geophysical Research Letters 46, 4230–4238.

Kowalik, Z., Proshutinsky, T., Proshutinsky, A., 2006. Tide-tsunami interactions. Science of Tsunami Hazards 24, 242–256.

Maksimov, M., Velímský, J., 2017. Fast calculations of the gradient and the hessian in the time-domain global electromagnetic induction inverse problem. Geophysical Journal International 210, 270–283.

Schmitz Jr, W.J., 1996. On the World Ocean Circulation: Volume 2 The Pacific and Indian Oceans/A Global Update. Technical Report. WOODS HOLE OCEANOGRAPHIC INSTITUTION MA.

Thébault, E., Finlay, C.C., Beggan, C.D., Alken, P., Aubert, J., Barrois, O., Bertrand, F., Bondar, T., Boness, A., Brocco, L., et al., 2015. International geomagnetic reference field: the 12th generation. Earth Planets Space 67, 1–19.

Tyler, R.H., Boyer, T.P., Minami, T., Zweng, M.M., Reagan, J.R., 2017. Electrical conductivity of the global ocean. Earth Planets Space 69, 156.

Velímský, J., 2013. Determination of three-dimensional distribution of electrical conductivity in the Earth's mantle from Swarm satellite data: Time-domain approach. Earth Planets Space 65, 1239–1246.